PHYSICAL REVIEW MATERIALS **8**, 084411 (2024)

Magnetic phase dependency of the thermal conductivity of FeRh from thermoreflectance experiments and numerical simulations

A. Castellano,[1] K. Alhada-Lahbabi,[2] J. A. Arregi,[3] V. Uhlíř,[3,4] B. Perrin,[2] C. Gourdon,[2] D. Fournier,[2]
M. J. Verstraete,[1,5] and L. Thevenard[2,*]
[1]*NanoMat/Q-Mat Université de Liège, and European Theoretical Spectroscopy Facility, B-4000 Liège, Belgium*
[2]*Sorbonne Université, CNRS, Institut des Nanosciences de Paris, 4 Place Jussieu, 75252 Paris, France*
[3]*CEITEC BUT, Brno University of Technology, Purkyňova 123, 612 00 Brno, Czech Republic*
[4]*Institute of Physical Engineering, Brno University of Technology, Technická 2, 616 69 Brno, Czech Republic*
[5]*Institute for Theoretical Physics, Physics Department, Utrecht University, 3508 TA Utrecht, The Netherlands*

(Received 25 May 2023; revised 27 June 2024; accepted 30 July 2024; published 28 August 2024)

FeRh is well known in its bulk form for a temperature-driven antiferromagnetic (AFM) to ferromagnetic (FM) transition near room temperature. It has aroused renewed interest in its thin-film form, with particular focus on its biaxial AFM magnetic anisotropy which could serve for data encoding, and the possibility to investigate laser-assisted phase transitions, with varying contributions from electrons, phonons, and magnons. In order to estimate the typical temperature increase occurring in these experiments, we performed modulated thermoreflectance microscopy to determine the thermal conductivity κ of FeRh. As often occurs upon alloying, and despite the good crystallinity of the layer, κ was found to be lower than the thermal conductivities of its constituting elements. More unexpectedly, given the electrically more conducting nature of the FM phase, it turned out to be three times lower in the FM phase compared to the AFM phase. This trend was confirmed by examining the temporal decay of incoherent phonons generated by a pulsed laser in both phases. To elucidate these results, first- and second-principles simulations were performed to estimate the phonon, magnon, and electron contributions to the thermal conductivity. They were found to be of the same order of magnitude, and to give a quantitative rendering of the experimentally observed κ_{AFM}. In the FM phase, however, simulations overestimate the low experimental values, implying very different (shorter) electron and magnon lifetimes.

DOI: 10.1103/PhysRevMaterials.8.084411

I. INTRODUCTION

The FeRh alloy with near equiatomic composition is a unique magnetic material, studied long ago in bulk form [1,2], and which has recently sparked a renewed interest in the thin-film form for technological applications. The first-order metamagnetic phase transition of FeRh from the antiferromagnetic (AFM) to the ferromagnetic (FM) state happens close to room temperature, and the associated changes in magnetic, electrical, and thermodynamic properties have been utilized to propose novel approaches for memory cells [3], heat-assisted magnetic recording [4], and magnetic refrigeration [5]. FeRh thin films are also good candidates to investigate laser-assisted transient [6–12] or irreversible [13] phase transitions.

Excitation of the AFM phase by a femtosecond laser pulse generates an out-of-equilibrium population of electrons and then phonons, whose temperatures eventually equilibrate, typically on picosecond timescales. The respective roles of electrons and phonons at the onset of a transient FM state are still much debated [7,8,10,11,14–16]. After this initial step on the picosecond timescale the local temperature decreases through heat diffusion. This evolution determines the nucleation, expansion and coalescence of FM domains as well as the decay of the transient magnetic moment upon cooling back to the AFM phase [12]. However, the heat diffusion coefficient D of FeRh is poorly known. It is related to the thermal conductivity κ by $D = \kappa/(\rho C)$, where ρ is the mass density and C the specific heat. Both ρ and C are known to vary with temperature and magnetic phase [17,18]. The heat conductivity also determines the stationary temperature rise of the sample when the pulsed laser repetition rate is too high for the system to relax back to its base temperature between pulses [6,8,19–21], or when a cw laser or current is used to induce a local nucleation of FM domains [13,22]. Whereas specific heat measurements are reported for FeRh bulk [1,2,23] and thin-film samples [18], the thermal conductivity is usually estimated from the electrical conductivity σ using the Wiedemann-Franz law $\kappa_e = L_0 T\sigma$, with L_0 being the Lorenz number [7]. A noteworthy exception is a recent paper by Ahn *et al.* [21] in which they evaluate indirectly $\kappa_{\mathrm{AFM}} = 11.8$ and $\kappa_{\mathrm{FM}} = 22.4\ \mathrm{W\,m^{-1}\,K^{-1}}$.

There are numerous reports of the material's electronic and phononic band structures, some giving calculations of its thermal proprieties [24–29]. Since FeRh is metallic, one could expect the electronic contribution to the thermal conductivity κ_e to be dominant over the phononic and magnonic (κ_{ph}, κ_m) ones, and to govern how κ should scale between its two magnetic phases. Relating in first approximation κ_e

---

[*] Contact author: thevenard@insp.jussieu.fr

2475-9953/2024/8(8)/084411(14)

to the electrical conductivity using the Wiedemann-Franz law mentioned above gives a value almost twice larger in the FM phase as in the AFM phase [30]. As for the phononic contribution, recent density functional theory (DFT) calculations by Cazorla and Rurali [28] predict it to be very slightly smaller in the AFM than in the FM phase. Finally, there is no record yet—either experimental or numerical—for the magnonic contribution κ_m. In pure bcc Fe it has been estimated to represent about 10% of the total thermal conductivity [31]. Overall, calculations so far suggest the FeRh FM phase to be thermally more conductive than the AFM one.

In this paper we determine the total thermal conductivity of a 195-nm-thick FeRh thin film, using modulated thermoreflectance (TR) microscopy. It is an ideal technique to measure the thermal properties of thin films deposited on a substrate, when the volume is too small to be probed by standard calorimetry techniques [32–35]. This enables us to estimate quantitatively transient and stationary laser-driven temperature rises. We confirm the results on thermal conductivity by monitoring the time decay of interferometric measurements in a pump-probe setup in both AFM and FM phases. In parallel, we compute the electronic, magnetic, and vibrational properties of the material, and the different contributions to the thermal conductivity in both phases. We then discuss how the total value compares to our data.

II. SAMPLE

An FeRh film with a thickness of $h = 195$ nm was deposited on a 500-μm-thick MgO(001) substrate via magnetron sputtering of an equiatomic FeRh target. The film was grown at 430 °C after preheating the substrate for 60 min at the same temperature. We used an Ar pressure of 2.7×10^{-3} mbar and a sputtering power of 50 W, leading to a deposition rate of 2 nm min^{-1}. Postgrowth annealing in high vacuum at 780 °C for 80 min yielded a good quality and homogeneous CsCl-type structure of the film [17]. It is nearly fully relaxed, with a +0.03% strain in the out-of-plane direction at room temperature. Finally, a 2-nm-thick Pt cap was grown after cooling the sample below 120 °C, to protect the film from oxidation. Please refer to Ref. [17] for a full structural characterization of a very similar sample.

The temperature-dependent magnetization data of the film measured via vibrating sample magnetometry (VSM) (Fig. 1) show a heating transition from AFM to FM state between 87 °C and 108 °C (360 and 381 K), and a cooling transition between 100 °C and 80 °C (373 and 353 K). The very weak residual ferromagnetic contribution in the AFM phase (4% of the magnetization at 400 K) is a signature of the excellent quality of the sample. The AFM-FM transition can also be monitored locally by reflectance microscopy at variable temperature. For this the sample is glued with thermal paste on the holder of a Linkam cryostat adapted to a microscopy setup. As expected for FeRh [36–38], a 3–4% hysteretic change of the phase-dependent reflectance $R(T)$ is observed at the AFM-FM transition (Fig. 1). The slight difference in shape and position of the transition compared to the curve measured by VSM reflects the much smaller probed volume (a few μm^2 wide, and about 10 nm deep) and the spatial variations of the magnetic properties.

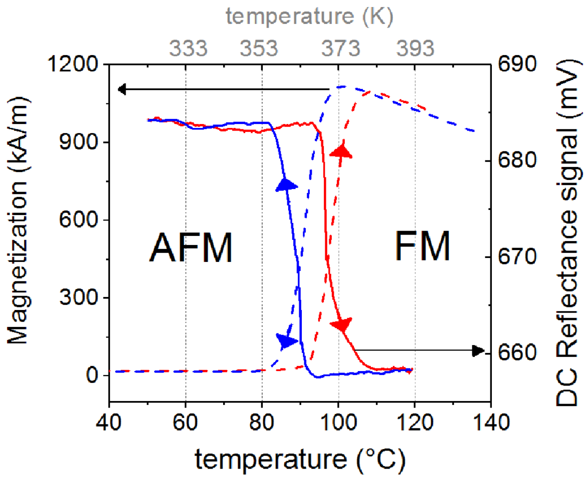

FIG. 1. Determination of the transition temperature of the film. Left: Global measurement of magnetization using vibrating sample magnetometry (dashed line). Right: Local measurement of the DC reflectance (continuous line) under probe beam only (λ = 488 nm, 0.8 μm spatial resolution) with a temperature ramp of 2 K/min.

III. MODULATED THERMOREFLECTANCE EXPERIMENTS: METHODOLOGY AND RESULTS

We now briefly describe the home-built thermoreflectance microscope that allows access to the thermal properties of the sample.

Light from a λ = 488 nm (blue) cw laser (probe beam) is focused onto its surface to a diffraction-limited spot by a 50× long-working-distance objective (numerical aperture NA = 0.5, working distance 10.6 mm). The typical power impinging on the sample is 120 μW. A heat source is provided by a 532-nm (green) cw laser passing through an acousto-optic modulator driven by a square modulation at frequency f and focused onto the sample by the objective (≈5.3 mW on the sample). This green laser spot is raster scanned on the sample surface while the reflected blue probe beam is collected by the photodiode which monitors the reflectance of the layer [Fig. 2(a)]. The green light reflected back towards the detector is blocked by an interference filter. The signal is fed into a lock-in amplifier that returns the amplitude and phase of the AC component of the reflectance at the frequency of the modulated heat source, ΔR_f, as well as the DC component R_0 thanks to an analog-to-digital converter (ADC). A typical map

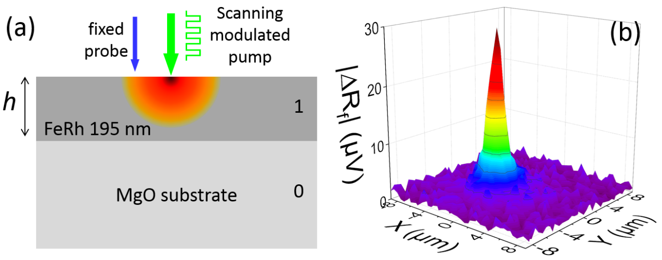

FIG. 2. (a) Schematic of the modulated thermoreflectance set-up. (b) 10×10 μm^2 map of the amplitude of the modulated thermoreflectance signal.

of the modulated reflectance is shown in Fig. 2(b) (amplitude component).

As described in detail in Ref. [32], the reflectance is assumed to depend on the temperature increase to the first order, $R(\mathbf{r},t) = R_0 + \frac{\partial R_{\text{probe}}}{\partial T} I_{\text{probe}}(\mathbf{r}) * \Delta T(\mathbf{r},t)$, where the temperature profile is convolved with the probe spot profile $I_{\text{probe}}(\mathbf{r})$. The modulated reflectance ΔR_f at frequency f reflects the f harmonic of the temperature increase ΔT_f induced by the pump laser. Modulation frequencies are moreover assumed to be low enough to consider the system at thermodynamic equilibrium, with the thermal flux being proportional to the temperature gradient [32]. Adapting Ref. [39] and using cylindrical coordinates, the thermal field at the surface of the sample and the modulated reflectance are given by inverse Hankel transforms as detailed in Eqs. (1)–(3):

$$\Delta T_f(r) = \frac{Q_f}{2\pi} \int_0^\infty g(u) J_0(ur) u \exp\left(-\frac{d_{\text{pump}}^2 u^2}{32}\right) du, \tag{1}$$

$$\Delta R_f(r) \propto \frac{\partial R_{\text{probe}}}{\partial T} \int_0^\infty g(u) J_0(ur) u A(u) \exp\left(-\frac{d_{\text{pump}}^2 u^2}{32}\right) du, \tag{2}$$

$$g(u) = \frac{\alpha^2}{\alpha^2 - \Sigma_1^2} \frac{\left(1 - \frac{\kappa_0^* \Sigma_0}{\kappa_1 \alpha}\right)(\cosh(\Sigma_1 h) - \exp(-\alpha h)) + \left(\frac{\kappa_0^* \Sigma_0}{\kappa_1 \Sigma_1} - \frac{\Sigma_1}{\alpha}\right) \sinh(\Sigma_1 h)}{\kappa_0^* \Sigma_0 \cosh(\Sigma_1 h) + \kappa_1 \Sigma_1 \sinh(\Sigma_1 h)}, \tag{3}$$

where $\Sigma_i(u,f) = \sqrt{u^2 + j\frac{2\pi f}{D_i}}$ is akin to a complex thermal wave vector ($j = \sqrt{-1}$). Indices 0 and 1 refer to the MgO substrate and the FeRh thin film, respectively. $D_i = \kappa_i/(\rho_i C_i)$ is the heat diffusivity with ρ_i and C_i the mass density and specific heat, respectively. $Q_f = \frac{4}{\pi} P_{\text{inc}}(1-R)$ is the f component of the incoming modulated heat power with R the reflection coefficient at the pump wavelength. J_0 is the Bessel function of the first kind, and α is the absorption coefficient of the pump beam in FeRh [40]. The last two terms of Eq. (2) describe the finite diameter of the laser spots: $A(u)$ is the Hankel transform of the Airy pattern of the diffraction-limited probe spot, and d_{pump} is the diameter at which the intensity of the Gaussian pump spot has fallen by e^2. Details and numerical values for known parameters are given in Appendix A.

The temperature increase includes *all* contributions to the thermal conductivity: phononic, electronic, magnonic, as well as the effect of any thermal interface resistance (TIR) R_{th} between the substrate and the thin film due to a localized scattering of phonons. Taking into account the presence of a TIR amounts to using in Eq. (3) a modified thermal conductivity for the substrate $\kappa_0^* = \kappa_0/(1 + R_{\text{th}}\kappa_0\Sigma_0)$ [41]. We now discuss possible values to give to R_{th}. The TIR is notoriously complicated to measure reliably [42], particularly in the case of a thermally insulating film/conducting substrate configuration. It may have *intrinsic* origins such as Umklapp processes [43], or, more likely at play in our case, *extrinsic* origins such as interface roughness—expected to be minute in our epitaxial films. Applying the diffuse mismatch model to the FeRh/MgO interface yields $R_{\text{th}} \sim 4\times10^{-9}$ m^2 K W^{-1} for both magnetic phases (see below for numerical details on this simulation). This method is known to give a lower bound for thermal interface resistance, but matches reassuringly well with experimental values found in the literature for thin metallic films (e.g., Al or Cu) deposited on an electrically insulating substrate (e.g., SiO_2 or Al_2O_3) [44,45]. It is also quite close to the value (2×10^{-9} m^2 K W^{-1}) estimated indirectly for antiferromagnetic FeRh/MgO by Ahn *et al.* [21].

Modulated thermoreflectance spatial scans measured on FeRh/MgO are typical of a thermal insulator over conducting substrate configuration. In this case, heat diffuses rapidly to the substrate, and then back to the top layer. To illustrate this, we plot in Fig. 3(a) the amplitude of the temperature rise given by Eq. (1) at an example frequency of $f = 250$ kHz, with and without an FeRh layer ($h = 0$ or 195 nm). Far from the center, the behavior of the MgO substrate is recovered, with the slope essentially governed by the frequency-dependent thermal diffusion length $\mu_0 = \sqrt{\frac{D_0}{\pi f}}$. The central temperature rise, on the other hand, roughly scales as $\frac{h}{\kappa_1} + R_{\text{th}}$ above the signal from the substrate [Fig. 3(a)]. As a result, it is (i) quite challenging to measure reliably the thermal conductivity of very thin and highly conductive films, and justifies the use of a fairly thick (195 nm) film for this study, and (ii) almost impossible to determine independently R_{th} and κ_1, as the two terms always appear together [46]. To analyze our data, we thus chose to impose a value for R_{th} (see discussion above). Finally, we verified that the $r = 0$ value of the amplitude scales linearly with the incident power.

In order to evaluate the thermal conductivity of FeRh at a given temperature, we record spatial scans of the amplitude and phase of the modulated thermoreflectance signal at three modulation frequencies (typically 100, 250, and 500 kHz), as shown for instance for $T = 100\,^{\circ}$C (373 K) in Figs. 3(b) and 3(c). We then perform a global fit of the logarithm of the normalized amplitude of the three curves, with the thermal conductivity of FeRh being the only free (shared) parameter and the pump beam diameter and TIR imposed. Starting from an identical value of $R_{\text{th}} = 4\times10^{-9}$ m^2 K W^{-1} in both AFM and FM phases, we also explore the possibility of a much larger TIR in the FM phase, and use the quality of the fit to validate the chosen value. Note that no knowledge of $\frac{\partial R_{\text{probe}}}{\partial T}$ is necessary to extract κ_1 from this analysis, since it is the relative spatial variations of the f component of the reflectance that are of importance. Finally, complementary MATLAB simulations including a third layer in the model

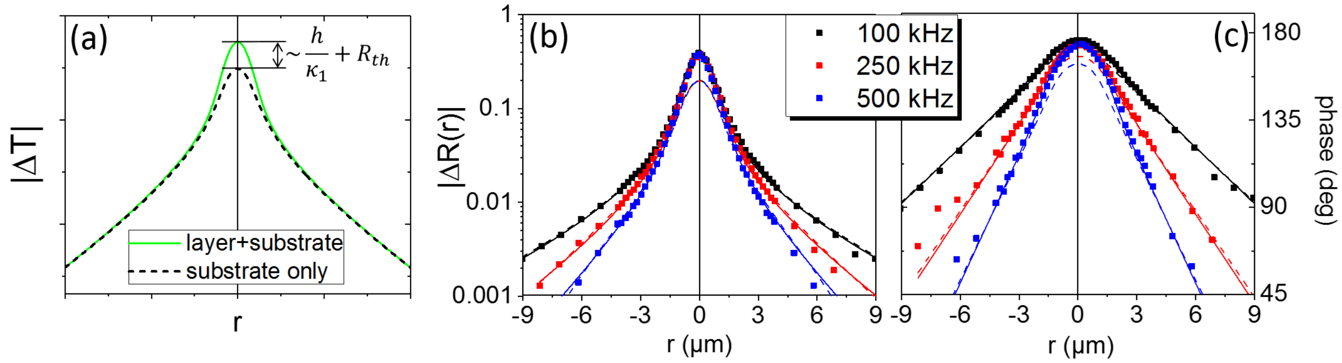

FIG. 3. (a) Illustration of the effect of the presence of a thin film over a better thermally conducting substrate: logarithm of the temperature rise induced by a 250 kHz modulated laser, with and without the 195-nm-thick FeRh film [Eq. (1)]. The "nose" contains information on the layer's thermal conductivity and on the thermal interface resistance. (b), (c) Experimental spatial scans of amplitude and phase taken at three modulation frequencies in the uniform FM phase ($T = 100\,^\circ\mathrm{C}$, 373 K). The fit of $\log|\Delta R|$ by Eq. (2) yields $\kappa_1 = 10 \pm 1$ W m^{-1} K^{-1}. The responses of the FeRh/MgO system (solid line) and MgO substrate only (dashed line) are plotted using $d = 2.1$ μm and $R_{\mathrm{th}} = 4\times10^{-9}$ m^2 K W^{-1}.

confirm that we can neglect the presence of the thin Pt cap in the analysis of the data.

Table I shows the final temperature dependence of the thermal conductivity of the 195-nm-thick FeRh film, established using the group fit procedure described above. The overall trend is distinctly that of a smaller value of $\kappa_1(T)$ in the FM phase compared to the AFM phase. More specifically, κ_1 is 25–30 W m^{-1} K^{-1} in the AFM phase, and around 10 W m^{-1} K^{-1} in the FM phase, i.e., almost three times less. This shows up clearly when plotting together spatial scans measured at the highest AFM temperature (60 °C) and lowest FM temperature (100 °C), in Fig. 4. The "nose" of the AFM spatial scan is strikingly smaller than in the FM scan. This could either be due to a smaller thermal conductivity in the FM phase, or to a much larger interface resistance. To test the latter hypothesis, we fit the FM data imposing a very large value of $R_{\mathrm{th}} = 4\times10^{-8}$ m^2 K W^{-1} (red curves in Fig. 5). This does yield a higher $\kappa_{1,\mathrm{FM}}$ of around 20 W m^{-1} K^{-1}, but at the cost of a poorer fit quality, particularly visible on the phase [Fig. 5(b)]. Note that this method sets an *upper* boundary to a likely value for R_{th}, while DFT simulations will give a lower limit.

We can now estimate the heat diffusivity $D_1 = \frac{\kappa_1}{\rho_1 C_1}$ of FeRh in both phases. Since the volume density of FeRh, ρ_1, varies appreciably with the magnetic phase (AFM or FM; see Appendix A for numerical values), D_1 is divided by over two upon crossing the transition: from $\sim 8\times10^{-6}$ m^2 s^{-1} in the AFM phase at 5 °C, to $\sim 3\times10^{-6}$ m^2 s^{-1} in the FM phase at 130 °C (403 K). Note that the former value is in the range of the diffusivity of 2×10^{-5} m^2 s^{-1} found by Bergman *et al.* [8] by fitting the laser-induced transient reflectivity, late after the arrival of the pulse, when the layer is back into its AFM phase. This makes FeRh roughly as heat diffusive as MgO in its AFM phase, but almost four times less in the FM phase. Typical thermal diffusion lengths at 500 kHz are then of a few microns, much more than the film thickness, but of the order of the diffraction-limited probe spot. This is known to lead in certain cases to an underestimation of the thermal conductivity, since higher mean-free path phonons will not contribute to the detected signal [47,48]. The apparent thermal conductivity is then found to *decrease* with *increasing* modulation frequency. However, we did not observe any particular tendency of the fitted thermal conductivity when performing single-scan fits in either phase, with a modulation frequency varying between 100 and 750 kHz.

Finally, a rough estimate in a one-dimensional (1D) approximation moreover gives the typical time it takes for the

TABLE I. Thermal conductivity extracted from group fits of the logarithm of the amplitude of the modulated reflectivity, imposing $R_{\mathrm{th}} = 4\times10^{-9}$ m^2 K W^{-1} as explained in the text.

Temperature (°C)	Phase	Thermal conductivity (W m^{-1} K^{-1})
5	AFM	26 ± 3
40	AFM	30 ± 5
60	AFM	30 ± 5
100	FM	10 ± 1
130	FM	9 ± 1

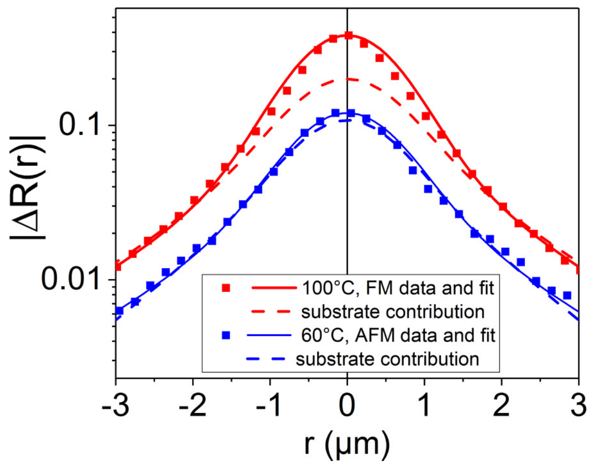

FIG. 4. Amplitude of the modulated reflectivity measured at 500 kHz in the uniform AFM (FM) phases at $T = 60\,^\circ\mathrm{C}$ in blue symbols ($T = 100\,^\circ\mathrm{C}$ in red symbols). Solid lines are fits to the data with $\kappa_1 = 30$ W m^{-1} K^{-1} (AFM) and $\kappa_1 = 10$ W m^{-1} K^{-1} (FM), while the dashed line is the contribution of the MgO substrate.

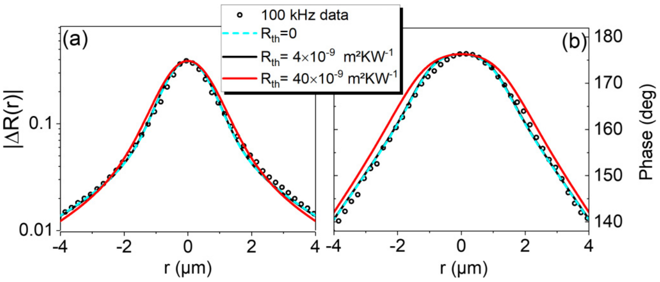

FIG. 5. (a) Amplitude and (b) phase at 100 kHz modulation frequency in the uniform FM phase ($T = 100\,^{\circ}$C, 373 K). Fitting the data with different thermal interface resistances $R_{\text{th}} = 0$, 4 or 40×10^{-9} m^2 K W^{-1} gives $\kappa_1 = 9$, 10, or 20 W m^{-1} K^{-1} (respectively green, blue, and red curves). The amplitude and phase are then calculated with Eq. (2). Note that the difference between the $R_{\text{th}} = 0$ and 40×10^{-9} m^2 K W^{-1} curves is minute on the amplitude data, but that the agreement with the phase data is poor for the larger TIR.

heat to escape laterally a $d \approx 2$ µm diameter heat spot as $\tau \approx \frac{d^2}{D_1}$, i.e., $\tau_{\text{AFM}} \approx 500$ ns while $\tau_{\text{FM}} \approx 1.2$ µs.

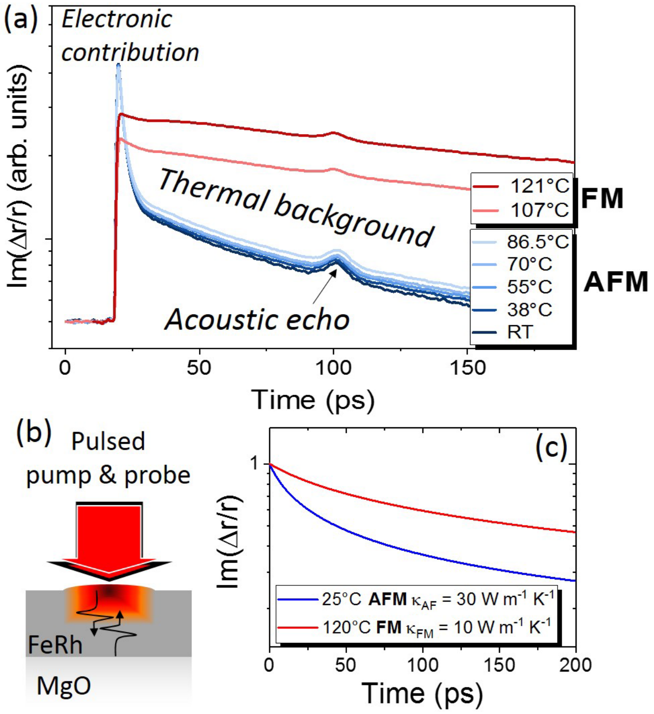

FIG. 6. (a) Interferometric signal at different temperatures on either side of the transition obtained using (b) a time-resolved pump-probe setup [47], with large-diameter spots. Incoherent phonon generation occurs together with the launching of a thermoelastically generated *coherent* strain wave that travels rapidly to the FeRh/MgO interface and back. The more rapid decay of the thermal background in the AFM phase indicates a higher thermal conductivity as evidenced from (c) the calculated interferometric signal, given by Eq. (4) and normalized to its $t = 0$ value.

IV. CONFIRMATION OF $\kappa_{\text{AFM}} > \kappa_{\text{FM}}$ USING PULSED GENERATION OF INCOHERENT PHONONS

The analysis of the thermoreflectance data points to a smaller thermal conductivity in the FM phase compared to the AFM phase, even considering a larger thermal interface resistance at high temperature. This comes as a surprising result given that both the Wiedeman-Franz law and a previous experimental estimate [21] seemed to indicate instead a larger thermal conductivity in the FM phase. To verify this, we performed picosecond acoustics pump-probe experiments (see Fig. 6, and Appendix B for experimental details). An 80-MHz femtosecond laser beam is split in a train of pump pulses that generate coherent strain waves by the thermoelastic effect, and delayed probe pulses that measure the dephasing of the reflected electric field of light by interferometry [49]. After an electronic signal decaying within 10–20 ps, one observes a slower decay related to the cooling of the layer as the heat is evacuated from the 12–13-nm-thick top layer in which the light has been absorbed [Fig. 6(a)]. It is clearly slower in the FM compared to the AFM phase, as it is also observed in the time-resolved strain measurements by Ahn *et al.* [21] (see in particular their supplemental information [50]). This indicates once more $\kappa_{1,\text{AFM}} > \kappa_{1,\text{FM}}$. We can this time safely discard the influence of the interface resistance on the thermal background during the $t_{\text{ps}} = 300$ ps window of observation: whereas the longitudinal acoustic wave traveling at 4741 m s^{-1} easily sees the FeRh interface twice, the thermal wave will only have reached around $l_{\text{th}} = \sqrt{Dt_{\text{ps}}} \approx 30$–50 nm deep into the FeRh layer. The interferometric signal is calculated as $\text{Im}(\Delta r(t)/r)$, where r is the amplitude reflection coefficient of the light electric field [Eq. (4), valid beyond the short-delay electronic peak]. The first term contains the surface displacement $u(t, z = 0)$. k_0 is the light wave vector, of norm $2\pi/\lambda$. The next term describes the reabsorption and dephasing of the reflected light, taking into account the change of the refractive index $n = n' + jn''$ induced by the propagating strain pulse S_{prop} and the temperature variation ΔT arising from heat diffusion:

$$\frac{\Delta r(t)}{r} = 2jk_0u(t, z = 0) + jk_0\frac{4n}{(1 - n^2)}\int_0^{\infty} \times\left(\frac{dn}{dS}S_{\text{prop}}(t, z) + \frac{dn}{dT}\Delta T(t, z)\right)\exp\left(j2k_0nz\right)dz. \tag{4}$$

The detailed expressions of $u(t, z = 0)$, $S_{\text{prop}}(t, z)$, and $\Delta T(t, z)$ and the parameters used in the modeling are given in Appendix B. The surface displacement and propagating strain are found to give smaller contributions to the interferometric signal as compared to heat diffusion. This signal is calculated using the thermal diffusivity given by κ values in Table I and shown in Fig. 6(c). It clearly evidences a faster decay in the AFM phase with a larger diffusivity, in good agreement with the experimental results of Fig. 6(a).

Finally, we briefly comment on the very different short-delay behavior observed in the AFM and FM phases: the electronic peak is almost suppressed in the latter configuration. The effect seems more related to the magnetic phase of the layer than to the temperature, since all AFM phase plots (from room temperature all the way to 86.5 °C) evidence the same sharp feature. At such a short delay, the signal does not reflect the surface displacement so much as variations of the electronic properties (band positions and/or optical index).

Although a detailed explanation of this effect is beyond the scope of this paper, we can suggest that the density of states of the less metallic AFM phase (see, e.g., Ref. [24]) presents many more empty states for electrons to be photoexcited into than in the FM phase. A similar correlation, between the short-delay peak in the reflectivity amplitude and electrical properties, has been observed on either side of metal-to-insulator transitions in $NdNiO_3$ [51] and $LaCaMnO_2$ [52].

V. DISCUSSION

Having confirmed the trend $\kappa_{1,\mathrm{AFM}} > \kappa_{1,\mathrm{FM}}$ seen on the modulated thermoreflectance data, we compare the values of the thermal conductivity in both phases (Table I) with that of other materials at room temperature. The absolute values are overall smaller than for [53] good metals (a few hundreds of $\mathrm{W\,m^{-1}\,K^{-1}}$), semiconductors ($\approx$10–100 $\mathrm{W\,m^{-1}\,K^{-1}}$), or even an electrical insulator such as MgO ($\approx$50 $\mathrm{W\,m^{-1}\,K^{-1}}$). As often occurs upon alloying [54], the thermal conductivity of FeRh is also smaller than those of its constituting single elements [53,55]: $\kappa_{\mathrm{Fe}} \approx 80\ \mathrm{W\,m^{-1}\,K^{-1}}$ and $\kappa_{\mathrm{Rh}} \approx 135\ \mathrm{W\,m^{-1}\,K^{-1}}$.

We can moreover estimate the stationary temperature increase due to the modulated green laser only, ΔT_{stat}, using Eq. (1) in which we set the frequency $f = 0$, $r = 0$, and the incoming heat flow as $Q_0 = P_{\mathrm{inc}}(1 - R)$. For an incident average laser power of $P_{\mathrm{inc}} \approx 5.3$ mW, the stationary temperature rise in the very center of a 2-μm-diameter pump spot will thus be of $\Delta T_{\mathrm{stat}} \approx 13\,^{\circ}\mathrm{C}$ for a base temperature of 40 °C or 60 °C (313 or 333 K) in the AFM phase ($\kappa_1 \approx 30\ \mathrm{W\,m^{-1}\,K^{-1}}$). Note that this estimate is strongly dependent on the pump spot diameter.

VI. CALCULATIONS OF κ_e, κ_{ph}, κ_m, AND R_{th}

To dissect the experimentally observed and counterintuitive thermal conductivity of FeRh, we perform simulations and combine with literature data to understand the individual phonon, electron, and magnon contributions for the FM and AFM phases.

A. Phonon thermal conductivity: Anharmonic phonon calculations

From an *ab initio* setting, the lattice contribution to the thermal conductivity can be computed by solving the phonon Boltzmann equation [56–58]. In order to obtain quantitative results, it is essential to include effects beyond the harmonic approximation, such as thermal expansion and intrinsic anharmonicity, in the description of the system. This seems to be particularly true for the AFM phase of FeRh, where previous theoretical studies predicted the appearance of an imaginary mode [24,59–61], which prevents the use of the harmonic approximation as a starting point for the Boltzmann equation. To go beyond the harmonic approximation, we employ the temperature-dependent effective potential (TDEP) method [58,62,63] to include anharmonicity and renormalize phonon-phonon interactions. To reduce the important simulation cost while keeping the accuracy of DFT, we constructed two machine learning interatomic potential (MLIP [64–66]) models of FeRh for the FM and AFM phases. The details of the simulations are described in Appendix C.

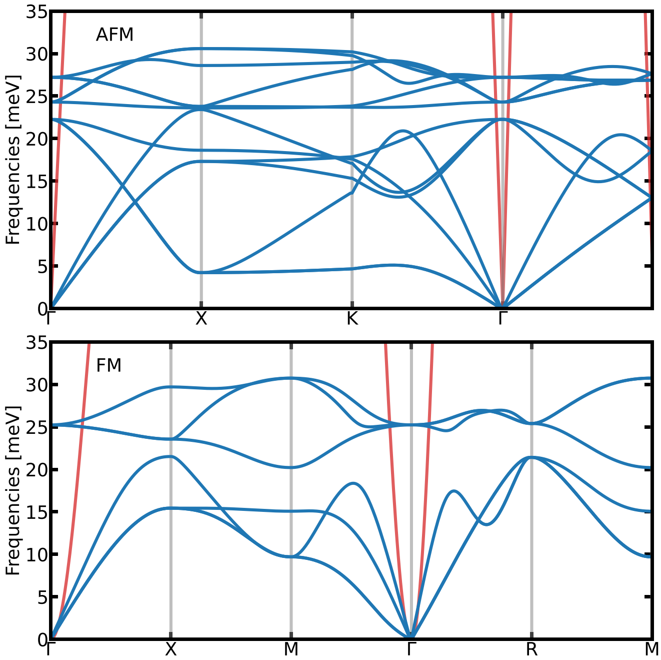

FIG. 7. Room-temperature phonon band structure for (top) the AFM and (bottom) the FM phase of FeRh. For comparison, the magnon band structures by Gu and Antropov [67] are also shown in red (assuming no magnetic anisotropy). The phonons in the FM phase are computed using the B2 structure as the unit cell, while the magnetic unit cell was used for the AFM phase.

The resulting renormalized phonon band structures at room temperature are represented in Fig. 7. In the FM phase, all Fe atoms are equivalent by symmetry, so that the magnetic unit cell coincides with the B2 structure which can be used to compute phonon-related properties. This is not the case for the AFM phase, where the spin-up or spin-down occupation of Fe atoms makes them inequivalent. Such a breaking of symmetry can have an important impact on the phonon properties [28]. To account for this effect, the phonons in the AFM phase were computed using the magnetic unit cell.

For both phases, we find that the spectra are fully real, demonstrating their dynamical stability. Some previous works [24,26] had suggested the possibility of an additional low-T phase for the AFM phase, which our results do not support (at least down to 50 K).

With these phonons and the third-order phonon scattering as input, we obtained the lattice thermal conductivity of the two phases using the iterative solution of the Boltzmann equation. Our results give $\kappa_{ph,\mathrm{AFM}} = 11.84\ \mathrm{W\,m^{-1}\,K^{-1}} > \kappa_{ph,\mathrm{FM}} = 10.36\ \mathrm{W\,m^{-1}\,K^{-1}}$ at room temperature. Our calculation differs from previous work in the literature [28], where the opposite trend was found. The thermal conductivities computed by Cazorla and Rurali [28] were based on the harmonic approximation at the ground-state volume and using a different exchange and correlation functional. We show in Appendix C that beyond the differences in the DFT calculations that are minor, the main difference in our results comes from the explicit variation of the interatomic force constants and volume with temperature. The difference in lattice κ_{ph} favors the AFM phase, but only slightly. However, the experimentally observed asymmetry between FM and AFM thermal conductivities also contains electronic and magnonic contributions to κ, which we proceed to estimate.

B. Electron thermal conductivity

The electronic thermal conductivity κ_e can be estimated from the charge conductivity σ, through the Wiedemann-Franz relationship. The latter is known not to hold universally, but breakdowns mainly appear for strongly correlated metals, strange band structures, or submicron structures [68]. In the present case if the Lorenz factor takes its ideal value of $L_0 = 2.44\times10^{-8}$ W Ω K^{-2}, we can extract the electron thermal conductivity as $\kappa_e = L_0 T\sigma$.

We measure the temperature-dependent resistance of a 195-nm-thick FeRh film which was grown together with the sample utilized for the thermoreflectance measurements above. The resistance measurement was carried out using the four-point probe method by contacting the film with four pins arranged in a square 4 mm on each side. The temperature was controlled using a custom-made Peltier holder and no magnetic field was applied during the measurement. In this way we find at 360 K $1/\sigma_{\rm AFM} = 1$ μΩ m and $1/\sigma_{\rm FM} = 0.6$ μΩ m, very close to values from the literature [69]. This implies $\kappa_{e,\rm AFM} \approx 9$ W m^{-1} K^{-1} which is sensibly lower than $\kappa_{e,\rm FM} \approx 15$ W m^{-1} K^{-1}. Theoretical calculations of κ_e in FeRh based on its electronic band structure also show a slightly larger value for the FM phase: Jimenez *et al.* [27] find $\kappa_{e,\rm AFM} \approx 21$ W m^{-1} K^{-1} and $\kappa_{e,\rm FM} \approx 27$ W m^{-1} K^{-1}, using a somewhat arbitrary temperature- and energy-independent relaxation time of 10^{-14} s. In their calculations the Lorenz factor is not presumed constant (and depends on the electronic band structure) but the κ_e is known only up to a rescaling by the relaxation time, which will be different for FM and AFM phases, and should be energy and/or state dependent. Overall, we expect $\kappa_{e,\rm FM}$ to be a bit larger than $\kappa_{e,\rm AFM}$, and of the order of 10–15 W m^{-1} K^{-1}.

C. Magnon thermal conductivity: Model dispersion and lifetime

Finally, we wish to estimate the magnon contribution to the thermal conductivity. Wu *et al.* [31] calculate simultaneous lattice and spin dynamics for bcc Fe, and find that the magnon contribution to κ ($\kappa_m = 15$ W m^{-1} K^{-1}) is larger than the lattice one ($\kappa_{ph} = 8$ W m^{-1} K^{-1}), though they are skeptical of their κ_m. We have reimplemented the magnon band model from Gu and Antropov [67] as a PYTHON script, and added the calculation of the group velocities $v_{q\lambda}$ and a lifetime given by $1/\tau_{q\lambda} = \alpha_G\omega_{q\lambda}$ which depends only on the frequency of mode λ at wave vector q. Here α_G is the Gilbert damping parameter, which should vary with temperature and magnetic ordering (and in principle also with the magnon mode λ, q). Using these ingredients, one can calculate the thermal conductivity with a formula analogous to that for phonons [Eq. (C2) in Appendix C]:

$$\tilde{\kappa}_m^{ab}(\omega) = \frac{1}{V}\sum_{q\lambda} v_{q\lambda}^a v_{q\lambda}^b C_\lambda(\omega_{q\lambda})\tau_{q\lambda}\delta(\omega - \omega_{q\lambda}), \tag{5}$$

$$\kappa_m^{ab} = \int \tilde{\kappa}_m^{ab}(\omega)\, d\omega, \tag{6}$$

where a and b are Cartesian components, C_λ is the mode specific heat (using the standard harmonic formula $C_\lambda = [x/(\sinh x)]^2$ with $x = \hbar\omega_{q\lambda}/2k_BT$), and V is the unit cell volume. We call $\tilde{\kappa}$ the spectral thermal conductivity. The q integrations are carried out numerically on 100^3 grid points for the primitive cubic Brillouin zone. In this framework, the band structure strongly favors $\kappa_{m,\rm FM}$, through the much larger density of states (DOS) at low frequency (quadratic vs linear dispersion), which boosts the C_v at low ω, where τ is also large. This effect is stronger than that of the magnon group velocities, which favor the AFM phase (constant acoustic velocity) over the FM phase (zero velocity at Γ which grows linearly). The product $C_v\tau v^2$ yields $\tilde{\kappa}_{m,\rm FM} \propto \omega^{1/2}$ for the FM phase, while $\tilde{\kappa}_{m,\rm AFM} \propto \omega$. The Bose distribution weights most of C_v and κ_m at low frequencies, generically favoring $\kappa_{m,\rm FM}$ over $\kappa_{m,\rm AFM}$.

An important ingredient of the calculation is the parameter α_G, in both phases. The only measurements of FeRh magnon damping have been performed in the uniform FM phase, for which quite a large spread has been reported. Intrinsic damping values of around 0.001–0.004 have been measured [70] or computed using a multiple scattering method including position and spin fluctuations [69]. Larger values between 0.03 and 0.1 have also been seen, and are attributed to the spin-sink effect of either an adjacent Pt layer [71], or residual AFM domains [72].

For the AFM phase, a first-principles calculation was made by Mahfouzi and Kioussis [73], and using their Eq. (5) we obtain values ranging from 0.03 to 0.3 between what they call low and high temperature. Simensen *et al.* [74] arrive at 0.3 with a magnon scattering theory.

Using a single conservative value $\alpha_G = 0.25$ for both phases, we obtain values of $\kappa_{m,\rm AFM} \sim 15$ W m^{-1} K^{-1} and $\kappa_{m,\rm FM} \sim 90$ W m^{-1} K^{-1}. The former is reasonable, but the latter is too large compared to our measurements. Examining the different ingredients for our model, the magnon dispersion compares favorably with experiments [75] and the calculations of Sandratskii and Buczek [76], except for a small but crucial underestimation of the FM phase stiffness at low frequency and q, noted by Castets *et al.* [75]. If the acoustic mode has a slight linear component (e.g., by mixing with phonon excitations) or much higher stiffness, the DOS, C_v, and $\kappa_{m,\rm FM}$ will be strongly reduced. The main source of uncertainty is the simplistic lifetime model as $1/\omega\alpha_G$: the large DOS and lifetimes at low frequency give too much weight to the FM-phase κ_m.

D. Estimate of the thermal resistance at the FeRh/MgO interface

The thermal interface resistance was estimated theoretically based on the bulk phonon dispersions of FeRh (FM and AFM) combined with those of MgO. The diffuse mismatch model (DMM) was used [77,78], which has two main hypotheses: (i) the phonons are transmitted based on their frequency matching and their group velocity component normal to the interface, and (ii) detailed balance and a steady state are achieved, which allows to calculate the transmission probability. The implementation was carried out in the ABINIT [79] package following the full phonon description in Ref. [80] and was benchmarked against their values for

TABLE II. Numerical estimates of the different contributions to the thermal conductivity. The last column refers to the total value, to be compared to the experimentally measured one (Table I).

Phase	κ_{ph}	κ_e	κ_m	κ (W m^{-1} K^{-1})
AFM	12	9	15	36
FM	10	15	90	115

interfaces between Si, Cu, and Al. For (100)-oriented FeRh on (100)MgO [81], the AFM phase has a room-temperature interface resistance of 4.3×10^{-9} m^2 K W^{-1}, and the FM phase of 4.2×10^{-9} m^2 K W^{-1}. While our layers are (001) oriented with excellent mosaicity [17], we mention that our calculations show that the resistance tends to decrease for other crystalline orientations, down to 2.3 (0.24) $\times10^{-9}$ m^2 K W^{-1} for FM (AFM) (111)FeRh on (111)MgO. The main factor boosting the interface resistance is the small overlap in frequency between light MgO and heavier FeRh. To fit the thermoreflectance spatial scans, we used the value $R_{\rm th} = 4\times10^{-9}$ m^2 K W^{-1}, but also considered the possibility of much larger values (see Fig. 5).

VII. DISCUSSION AND COMPARISON TO EXPERIMENTS

We find three comparable contributions for the thermal conductivity, between the lattice, electronic, and magnon terms (Table II). Each term has been estimated using available simulations or experimental input, and they are all on the order of 10 W m^{-1} K^{-1}, with $\kappa_{m,\rm FM}$ the only outlier. The sum renders quite nicely the measurements of $\kappa_{\rm AFM} \sim$ 30 W m^{-1} K^{-1}, but the lower measured $\kappa_{\rm FM}$ requires additional attention: the observed difference in the lattice κ_{ph} provides 1–2 W m^{-1} K^{-1}, but the other two terms favor FM over AFM.

Several factors may contribute to lower $\kappa_{\rm FM}$:

(1) The multidomain state of the layer in its FM phase could give an extra contribution from ferromagnetic domain-wall resistance [82], but a large number of ferromagnetic domains is quite unlikely under the two-micron spot, due to the competition between exchange and magnetostatic energy cost.

(2) Disorder will limit transport in both phases, but magnetic disorder (e.g., domains, impurities) will affect the FM phase transport more strongly as the dipolar interaction is longer ranged. The strong κ_m advantage of FM over AFM for long wavelengths will be reduced by defects and grain boundaries.

(3) The low-q magnon-phonon coupling is bound to play a critical role (see Fig. 7). Due to their quadratic dispersion and very similar frequencies, the FM magnons will interfere with acoustic phonons, limiting both lattice κ_{ph} and magnon κ_m. The impact of this coupling on the latter could have a significant impact on the total thermal conductivity on the FM phase. Compounding this effect, the AFM magnon group velocity is much higher and there will be no coupling of magnons to acoustic phonons.

(4) Our model for magnon lifetimes is quite crude, and may break down. Beyond the temperature and magnetic state, the "true" $\alpha_{G,q\lambda} = 1/\omega_{q\lambda}\tau_{q\lambda}$ will also depend on the specific magnon mode. It could also be impacted by an Fe:Rh stoichiometry varying from 1:1. It is known that magnetic properties vary steeply with this ratio. Any upper bound on the lifetimes at low q and low frequency will again reduce $\kappa_{\rm FM}$ more strongly.

VIII. CONCLUSIONS

Space- and frequency-dependent thermoreflectance measurements were performed in order to determine the thermal conductivity of a 195-nm-thick FeRh film in a wide temperature range of 5 °C to 130 °C, across the AFM-to-FM transition. Unexpectedly (based on rough estimates made with the Wiedemann-Franz law), the thermal conductivity is found overall three times *larger* in the AFM phase compared to the FM phase, a trend confirmed by the temporal decay of laser-pulsed generated incoherent phonons. These values were then used to estimate the expected transient and stationary temperature rises induced by a laser. To explain why the total FM thermal conductivity is lower than the AFM one, we estimated the phononic contribution to κ from anharmonic first-principles dynamics, the electronic contribution from the experimental resistivity using the Wiedemann-Franz law, and the magnonic contribution using a linear spin wave model from the literature, with a Gilbert-type relaxation time. In the AFM phase, the three components were found to be of the same order of magnitude, with a total of around 36 W m^{-1} K^{-1}, very close to the observed ≈30 W m^{-1} K^{-1}. In the FM phase, however, the calculated thermal conductivity rockets to ≈115 W m^{-1} K^{-1}, which is unrealistically large with regards to the observed ≈10 W m^{-1} K^{-1}. More accurate modeling of electronic and magnonic contributions will be required: in particular the large uncertainties in the magnetic damping, the magnon-phonon coupling, and the effects of disorder lead to a strong overestimate of the components of $\kappa_{\rm FM}$. Future experiments will be needed on the thermal conductivity in other FeRh layers, changing the thickness, polycristallinity, or strain, by growing them on substrates presenting a larger thermal contrast, e.g., silicon [32].

These results underscore the complexity of FeRh and the importance of the three-way couplings between electrons, phonons, and magnons, which are on equal footing in the total thermal conductivity.

ACKNOWLEDGMENTS

This work has been partly supported by the French Agence Nationale de la Recherche (ANR ACAF 20-CE30-0027). We acknowledge M. Vabre (Institut des Nanosciences de Paris) for technical assistance. Access to the CEITEC Nano Research Infrastructure was supported by the Ministry of Education, Youth and Sports (MEYS) of the Czech Republic under the project CzechNanoLab (LM2023051). A.C. and M.J.V. acknowledge the Fonds de la Recherche Scientifique (FRS-FNRS Belgium) for PdR Grant No. T.0103.19-ALPS, and ARC project DREAMS (G.A. 21/25-11) funded by Federation Wallonie Bruxelles and ULiege, and the Excellence of Science (EOS) program (Grant No. 40007563-CONNECT) funded by the FWO and F.R.S.-FNRS. Simulation time was awarded by the Belgian share of EuroHPC in LUMI hosted by CSC in Finland, by the CECI (FRS-FNRS Belgium Grant No. 2.5020.11), as well as the Zenobe Tier-1 of the Fédération Wallonie-Bruxelles (Walloon Region Grant Agreement No. 1117545).

APPENDIX A: PARAMETERS

The values for the thermal conductivity $\kappa_0(T)$, diffusivity $D_0(T)$, and specific heat $C_0(T)$ of MgO were taken from Ref. [83]. The specific heat $C_1(T)$ of FeRh was found in Ref. [1], where they measured much thicker, polycrystalline films. We believe any error in this parameter should impact only mildly the determination of κ_1. Indeed this parameter intervenes through the calculation of the diffusivity of FeRh, $D_1(T)$, which has a minor effect on the analysis of modulated thermoreflectance experiments in the “insulating-over-conductive layer” configuration [32]. The volume density of FeRh was taken phase dependent and temperature independent [84] from Ref. [24]: $\rho_{1,\mathrm{AFM}} = 9744.51\ \mathrm{kg\,m^{-3}}$ and $\rho_{1,\mathrm{FM}} = 9590.11\ \mathrm{kg\,m^{-3}}$. A standard knife-edge measurement in our experimental geometry gives $d_{\mathrm{pump}} = 2. \pm 0.1\ \mu\mathrm{m}$. The probe beam was taken as diffraction limited and described by the Hankel transform $A(u) = \arccos(\frac{u\lambda}{4\pi NA}) - \frac{1}{2}\sin(2\arccos(\frac{u\lambda}{4\pi NA}))$ with the probe wavelength $\lambda = 488$ nm here, and $NA = 0.5$ the numerical aperture of the objective. The reflectance of FeRh was taken phase dependent and estimated as $R_{\mathrm{AFM}} = 0.75$ and $R_{\mathrm{FM}} = 0.72$ by comparing to the reflectance of aluminum. Finally, the light absorption coefficient of FeRh was estimated in both phases by measuring the light reflected from or transmitted through a 30-nm sample grown in similar conditions. It corresponds to a penetration depth of around 10 nm (12–13 nm) at 532 nm (773 nm), much less than the thickness of the film $h = 195$ nm.

APPENDIX B: DETAILS ON THE PICOSECOND ACOUSTICS EXPERIMENTS AND MODELING

The picosecond acoustics pump-probe setup is described in Ref. [49]. More specifically to these measurements, the laser repetition rate was 80 MHz, with a modulation of 1 MHz. Its wavelength was 773 nm, and the beam diameter was of the order of ≈15 μm. The power of the pump beam was around $P = 32$ mW, and that of the probe was around 4 mW. The delay line was scanned mechanically at 40 nm/ps. The model is based on the 1D heat diffusion equation and the propagation equation for elastic waves. Given the short timescale (300 ps), the FeRh layer can be considered as a semi-infinite medium since the thermal wave has not reached the substrate. The surface displacement $u(t, z = 0)$, propagating strain $S_{\mathrm{prop}}(t, z)$, and temperature increase $\Delta T(t, z)$ are obtained as [85]

$$u(0,t) = -\frac{S_0}{\alpha}\left(1 - \frac{x\exp(-\omega_\alpha t)}{x+1} - \frac{x\exp(\omega_D t)}{x^2-1}\mathrm{Erfc}\left(\sqrt{\omega_D t}\right) + \frac{\exp(x\omega_\alpha t)}{x^2-1}\mathrm{Erfc}\left(\sqrt{x\omega_\alpha t}\right)\right), \tag{B1}$$

$$S_{\mathrm{prop}} = \begin{cases} z - vt > 0, & \frac{S_0}{1-x^2}(\exp(-\omega_D(z/v - t)) - x\exp(-\omega_\alpha(z/v - t))) \\ z - vt < 0, & \frac{S_0}{1-x^2}\left(\exp(\omega_D(t - z/v))\mathrm{Erfc}\left(\sqrt{\omega_D(t - z/v)}\right) - x\exp(x\omega_\alpha(t - z/v))\mathrm{Erfc}\left(\sqrt{x\omega_\alpha(t - z/v)}\right)\right), \end{cases} \tag{B2}$$

$$\Delta T(t,z) = \frac{F(1-R)\alpha}{2\rho_1 C_1}\exp(\omega_D t)\left(\exp(-\alpha z)\mathrm{Erfc}\left(\frac{-z + 2D_1\alpha t}{2\sqrt{D_1 t}}\right) + \exp(\alpha z)\mathrm{Erfc}\left(\frac{z + 2D_1\alpha t}{2\sqrt{D_1 t}}\right)\right), \tag{B3}$$

where α, D_1, v, ρ_1, C_1, and R, are the absorption coefficient, diffusivity, longitudinal acoustic velocity, mass density, specific heat, and reflectivity coefficient of FeRh, respectively. We take $\kappa_{\mathrm{AFM}}(\kappa_{\mathrm{FM}}) = 30(10)\ \mathrm{W\,m^{-1}\,K^{-1}}$, hence $D_{\mathrm{AFM}}(D_{\mathrm{FM}}) = 9.3(2.7)\times 10^{-6}\ \mathrm{m^2\,s^{-1}}$, and $v_{\mathrm{AFM}}(v_{\mathrm{FM}}) = 4741(4865)\ \mathrm{m\,s^{-1}}$ [86]. $F = 0.2\ \mathrm{mJ\,cm^{-2}}$ is the laser fluence. We note $\omega_\alpha = \alpha v$, $\omega_D = D_1\alpha^2$, and $x = \omega_\alpha/\omega_D$. The real and imaginary parts of the refractive index $n = n' + j\,n''$ were obtained at $\lambda = 773$ nm as a function of temperature by ellipsometry from 20 °C to 120 °C. For instance, at 25 °C for the AFM phase and 120 °C for the FM phase: $n'_{\mathrm{AFM}}(n'_{\mathrm{FM}}) = 4.1(4.2)$, $n''_{\mathrm{AFM}}(n''_{\mathrm{FM}}) = 5(4.4)$ and hence $\alpha_{\mathrm{AFM}}(\alpha_{\mathrm{FM}}) = 8.1(7.2)\times 10^7\ \mathrm{m^{-1}}$. The derivatives are $dn'_{\mathrm{AFM}}/dT(dn'_{\mathrm{FM}}/dT) = 7.6(6.8)\times 10^{-3}$ and $dn''_{\mathrm{AFM}}/dT(dn''_{\mathrm{FM}}/dT) = 4(2.8)\times 10^{-3}$. S_0 is defined as $3\beta B\alpha(1-R)F/(\rho_1^2 C_1 v^2)$, where β is the thermal expansion coefficient and B the bulk modulus. Using data from Refs. [21,86] we have $S_{0\mathrm{AFM}}(S_{0\mathrm{FM}}) = 3.8(2)\times 10^{-4}$. The derivative dn/dS is not known but, taking a large value of 30 consistent with data from the literature [87], we get a smaller contribution of the propagating strain in the interferometric signal.

APPENDIX C: METHOD AND COMPUTATIONAL DETAILS FOR LATTICE THERMAL CONDUCTIVITY

1. Temperature-dependent effective potential

The temperature-dependent effective potential [58,62,63] method is based on the construction of an effective anharmonic Hamiltonian of the form

$$H = \sum_i \frac{p_i^2}{2M_i} + \frac{1}{2}\sum_{ij}\sum_{ab}\Theta_{ij}^{ab}u_i^a u_j^b + \frac{1}{3!}\sum_{ijk}\sum_{abc}\Psi_{ijk}^{abc}u_i^a u_j^b u_k^c, \tag{C1}$$

where u_i^a and p_i are respectively the displacement along the Cartesian direction a and momentum of atom i with mass M_i, and Θ_{ij}^{ab} and Ψ_{ijk}^{abc} are the second- and third-order interatomic force constants, which we fit to molecular dynamics data using ordinary least-squares methods. The effectiveness of this Hamiltonian comes from the iterative nature of the fit, where each order is fit on the residual of the previous order. While this procedure ensures that the lowest orders intrinsically include most of the anharmonicity, it also produces, as the name suggests, a temperature-dependent effective potential, so that individual molecular dynamics (MD) simulations have to be run for each temperature of interest.

Once the interatomic force constants are extracted from MD simulations, the thermal conductivity can be computed using the Boltzmann equation. In this work, the solution of this equation was obtained with an iterative algorithm [56], after which the thermal conductivity tensor is written as

$$\kappa_{ph}^{ab} = \frac{1}{V}\sum_{\lambda} C_\lambda v_\lambda^a F_\lambda^b, \tag{C2}$$

with V the volume of the unit cell, C_λ the heat capacity associated with mode λ, v_λ^a the group velocity of mode λ along Cartesian direction a, and F_λ^a the nonequilibrium phonon distribution accounting for the phonon relaxation, for which the Boltzmann transport equation must be solved self-consistently. The Boltzmann equation was solved on a $25\times25\times25$ **q**-point grid using an adaptive Gaussian scheme for the Dirac delta [88].

For both the extraction of the interatomic force constants and the computation of the thermal conductivity, we used the implementation provided by the TDEP package [89].

2. Machine learning interatomic potential and molecular dynamics

To decrease the important computational cost associated with the MD simulations, we used two machine learning interatomic potentials (MLIPs) within the moment tensor potential [65] formalism, one for the AFM phase and the other one for the FM phase. The MLIPs were fit on DFT calculations performed with the ABINIT suite [79] using the Perdew-Burke-Ernzerhof (PBE) parametrization of the exchange and correlation functional [90] in the projector augmented wave (PAW) formalism [91,92]. These MLIPs were successfully used to study the elastic properties of FeRh and we refer to our previous work [86] for more details about the parameters and data set used in their construction.

With the MLIPs, we compute the effective anharmonic Hamiltonian from 100 to 500 K in steps of 100 K. For each temperature, we run two 100-ps MD simulations on $8\times8\times8$ supercells, with a time step of 1 fs using the LAMMPS package [93]. The first MD run is performed in the *NPT* ensemble, and is used to compute the average equilibrium volume, while the second one employs this equilibrium volume in the *NVT* ensemble, in order to compute the renormalized interatomic force constants. These force constants are computed using 900 uncorrelated configurations, extracted from the *NVT* MD trajectory after 10 ps of equilibration.

3. Temperature-dependent phonons

The temperature-dependent phonon dispersions of both phases are plotted in Fig. 8. For the FM phase, we observe only a slight softening of the phonon frequencies with an increase in temperature, indicating a relatively small anharmonicity in the system even at a temperature of 500 K. It should be noted that most of this temperature dependence can be attributed to the thermal expansion. While most of the modes in the AFM phase show similar behavior, this is not the case for the lowest energy mode located at the high-symmetry X point. This mode, which we find to be imaginary in the harmonic approximation (as in previous literature, e.g., Refs. [24,59–61]), has instead the opposite trend: a strong hardening with temperature. We note that even at 100 K, which is the lowest temperature studied here, this mode and the whole spectrum are fully real, demonstrating the stability of the AFM phase.

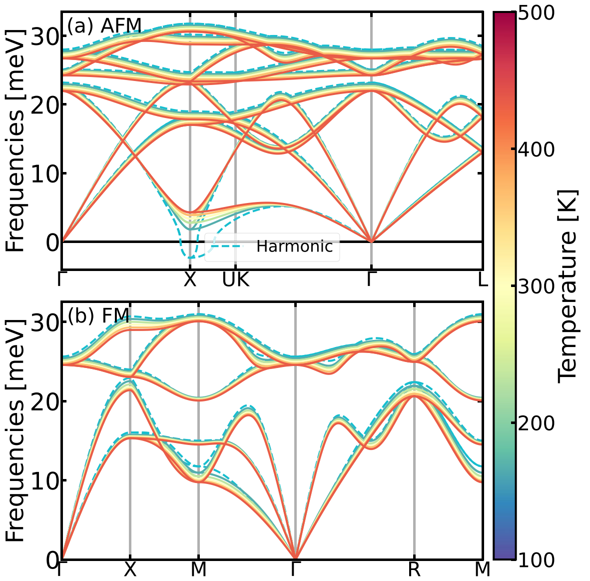

FIG. 8. Temperature-dependent phonons for (a) the FM and (b) the AFM phase of FeRh. In (b) the harmonic phonons are computed with finite difference to highlight the stabilization of the system by anharmonicity. The phonons in the FM phase are computed using the B2 structure as the unit cell, while the magnetic unit cell was used for the AFM phase.

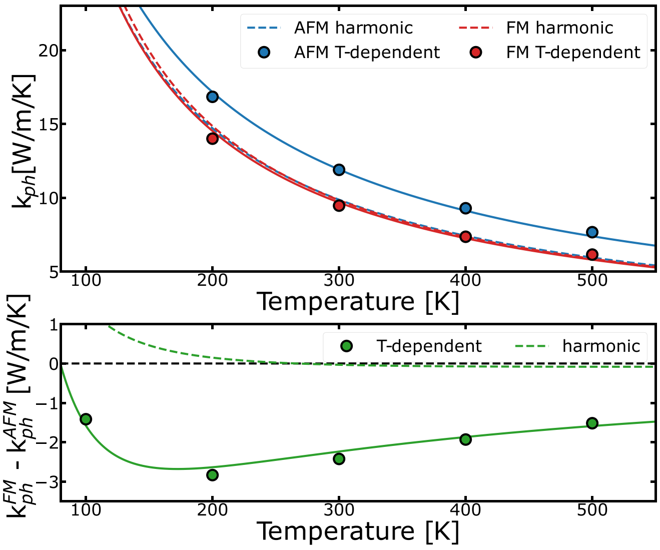

FIG. 9. (a) Theoretical lattice thermal conductivity of FeRh computed for the AFM phase, in blue, and the FM phase, in red. The harmonic results, represented with dashed lines, are obtained with IFC (Interatomic Force Constants) computed at $T = 25$ K. (b) Difference of thermal conductivity between the FM and the AFM phases.

Using these force constants as input, we computed the thermal conductivity by solving the iterative Boltzmann equation for each temperature. Our results, Fig. 9, show a slightly larger κ_{ph} for the AFM phase than for the FM phase above 150 K. As already stated in the main text, these findings differ from the results of Cazorla and Rurali [28], where the opposite trend was found based on the harmonic approximation at the 0 K relaxed volume. To better understand the origin of this discrepancy, we computed the thermal conductivities with our MLIP using analogous approximations. Due to the imaginary mode in the AFM phase, and in order to provide a meaningful comparison, we used IFC computed at a temperature of 25 K and at the reference relaxed volume for both phases, instead of the harmonic ones. As shown in Fig. 9, these approximations yield the same trend as in Ref. [28], with $\kappa_{ph,\mathrm{FM}} > \kappa_{ph,\mathrm{AFM}}$ for all temperatures. To explain the opposite trend obtained with fully anharmonic IFC, we compare the $T = 300$ K phonon lifetimes obtained with the two approaches in Fig. 10.

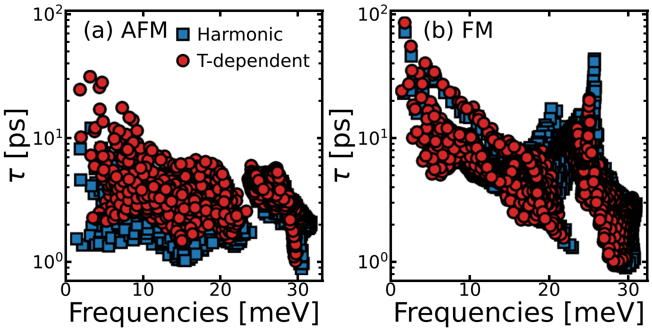

FIG. 10. Phonon lifetimes at 300 K in (a) the AFM phase and (b) the FM phase. In both panels, the harmonic results are taken without accounting for the temperature dependence of the phonons.

The FM phase presents only a slight evolution of the lifetimes, confirming the low anharmonicity of this phase. On the contrary, the renormalization of the IFC brings an important *increase* of the phonon lifetimes in the AFM phase. This counterintuitive effect can be understood as the decrease of the scattering phase space due to the renormalization of the phonons [94]. In the AFM phase of FeRh, this effect is sufficiently strong for $\kappa_{ph,\mathrm{AFM}}$ to exceed $\kappa_{ph,\mathrm{FM}}$.

---

[1] M. J. Richardson, D. Melville, and J. A. Ricodeau, Specific heat measurements on an FeRh alloy, Phys. Lett. A **46**, 153 (1973).

[2] M. P. Annaorazov, K. A. Asatryan, G. Myalikgulyev, S. A. Nikitin, A. M. Tishin, and A. L. Tyurin, Alloys of the FeRh system as a new class of working material for magnetic refrigerators, Cryogenics **32**, 867 (1992).

[3] X. Marti, I. Fina, C. Frontera, J. Liu, P. Wadley, Q. He, R. J. Paull, J. D. Clarkson, J. Kudrnovský, I. Turek, J. Kuneš, D. Yi, J.-H. Chu, C. T. Nelson, L. You, E. Arenholz, S. Salahuddin, J. Fontcuberta, T. Jungwirth, and R. Ramesh, Room-temperature antiferromagnetic memory resistor, Nat. Mater. **13**, 367 (2014).

[4] J.-U. Thiele, S. Maat, and E. E. Fullerton, FeRh/FePt exchange spring films for thermally assisted magnetic recording media, Appl. Phys. Lett. **82**, 2859 (2003).

[5] S. Cervera, M. Trassinelli, M. Marangolo, C. Carrétéro, V. Garcia, S. Hidki, E. Jacquet, E. Lamour, A. Lévy, S. Macé, C. Prigent, J. P. Rozet, S. Steydli, and D. Vernhet, Modulating the phase transition temperature of giant magnetocaloric thin films by ion irradiation, Phys. Rev. Mater. **1**, 065402 (2017).

[6] J. U. Thiele, M. Buess, and C. H. Back, Spin dynamics of the antiferromagnetic-to-ferromagnetic phase transition in FeRh on a sub-picosecond time scale, Appl. Phys. Lett. **85**, 2857 (2004).

[7] G. Ju, J. Hohlfeld, B. Bergman, R. J. M. van de Veerdonk, O. N. Mryasov, J.-Y. Kim, X. Wu, D. Weller, and B. Koopmans, Ultrafast generation of ferromagnetic order via a laser-induced phase transformation in FeRh thin films, Phys. Rev. Lett. **93**, 197403 (2004).

[8] B. Bergman, G. Ju, J. Hohlfeld, R. J. M. van de Veerdonk, J.-Y. Kim, X. Wu, D. Weller, and B. Koopmans, Identifying growth mechanisms for laser-induced magnetization in FeRh, Phys. Rev. B **73**, 060407(R) (2006).

[9] I. Radu, C. Stamm, N. Pontius, T. Kachel, P. Ramm, J.-U. Thiele, H. A. Dürr, and C. H. Back, Laser-induced generation and quenching of magnetization on FeRh studied with time-resolved x-ray magnetic circular dichroism, Phys. Rev. B **81**, 104415 (2010).

[10] F. Quirin, M. Vattilana, U. Shymanovich, A.-E. El-Kamhawy, A. Tarasevitch, J. Hohlfeld, D. von der Linde, and K. Sokolowski-Tinten, Structural dynamics in FeRh during a laser-induced metamagnetic phase transition, Phys. Rev. B **85**, 020103(R) (2012).

[11] S. O. Mariager, F. Pressacco, G. Ingold, A. Caviezel, E. Möhr-Vorobeva, P. Beaud, S. L. Johnson, C. J. Milne, E. Mancini, S. Moyerman, E. E. Fullerton, R. Feidenhans'l, C. H. Back, and C. Quitmann, Structural and magnetic dynamics of a laser induced phase transition in FeRh, Phys. Rev. Lett. **108**, 087201 (2012).

[12] F. Pressacco, D. Sangalli, V. Uhlíř, D. Kutnyakhov, J. A. Arregi, S. Y. Agustsson, G. Brenner, H. Redlin, M. Heber, D. Vasilyev, J. Demsar, G. Schönhense, M. Gatti, A. Marini, W. Wurth, and F. Sirotti, Subpicosecond metamagnetic phase transition in FeRh driven by non-equilibrium electron dynamics, Nat. Commun. **12**, 5088 (2021).

[13] A. B. Mei, I. Gray, Y. Tang, J. Schubert, D. Werder, J. Bartell, D. C. Ralph, G. D. Fuchs, and D. G. Schlom, Local photothermal control of phase transitions for on-demand room-temperature rewritable magnetic patterning, Adv. Mater. **32**, 2001080 (2020).

[14] G. Li, R. Medapalli, J. H. Mentink, R. V. Mikhaylovskiy, T. G. H. Blank, S. K. K. Patel, A. K. Zvezdin, Th. Rasing, E. E. Fullerton, and A. V. Kimel, Ultrafast kinetics of the antiferromagnetic-ferromagnetic phase transition in FeRh, Nat. Commun. **13**, 2998 (2022).

[15] M. Mattern, J. Jarecki, J. A. Arregi, V. Uhlíř, M. Rössle, and M. Bargheer, Speed limits of the laser-induced phase transition in FeRh, APL Mater. **12**, 051124 (2024).

[16] M. Mattern, J.-E. Pudell, J. A. Arregi, J. Zlámal, R. Kalousek, V. Uhlíř, M. Rössle, and M. Bargheer, Accelerating the laser-

induced phase transition in nanostructured FeRh via plasmonic absorption, Adv. Funct. Mater. **16**, 2313014 (2024).

[17] J. A. Arregi, O. Caha, and V. Uhlíř, Evolution of strain across the magnetostructural phase transition in epitaxial FeRh films on different substrates, Phys. Rev. B **101**, 174413 (2020).

[18] D. W. Cooke, F. Hellman, C. Baldasseroni, C. Bordel, S. Moyerman, and E. E. Fullerton, Thermodynamic measurements of Fe-Rh alloys, Phys. Rev. Lett. **109**, 255901 (2012).

[19] S. Shihab, L. Thevenard, A. Lemaître, J. Y. Duquesne, and C. Gourdon, Steady-state thermal gradient induced by pulsed laser excitation in a ferromagnetic layer, J. Appl. Phys. **119**, 153904 (2016).

[20] F. Pressacco, V. Uhlíř, M. Gatti, A. Nicolaou, A. Bendounan, J. A. Arregi, S. K. K. Patel, E. E. Fullerton, D. Krizmancic, and F. Sirotti, Laser induced phase transition in epitaxial FeRh layers studied by pump-probe valence band photoemission, Struct. Dyn. **5**, 034501 (2018).

[21] Y. Ahn, J. Zhang, Z. Chu, D. A. Walko, S. O. Hruszkewycz, E. E. Fullerton, P. G. Evans, and H. Wen, Ultrafast switching of interfacial thermal conductance, ACS Nano **17**, 18843 (2023).

[22] T. Moriyama, N. Matsuzaki, K.-J. Kim, I. Suzuki, T. Taniyama, and T. Ono, Sequential write-read operations in FeRh antiferromagnetic memory, Appl. Phys. Lett. **107**, 122403 (2015).

[23] B. Fogarassy, T. Kemény, L. Pál, and J. Tóth, Electronic specific heat of iron-rhodium and iron-rhodium-iridium alloys, Phys. Rev. Lett. **29**, 288 (1972).

[24] U. Aschauer, R. Braddell, S. A. Brechbühl, P. M. Derlet, and N. A. Spaldin, Strain-induced structural instability in FeRh, Phys. Rev. B **94**, 014109 (2016).

[25] W. He, H. Huang, and X. Ma, First-principles calculations on elastic and entropy properties in FeRh alloys, Mater. Lett. **195**, 156 (2017).

[26] M. Wolloch, M. E. Gruner, W. Keune, P. Mohn, J. Redinger, F. Hofer, D. Suess, R. Podloucky, J. Landers, S. Salamon, F. Scheibel, D. Spoddig, R. Witte, B. Roldan Cuenya, O. Gutfleisch, M. Y. Hu, J. Zhao, T. Toellner, E. E. Alp, M. Siewert *et al.*, Impact of lattice dynamics on the phase stability of metamagnetic FeRh: Bulk and thin films, Phys. Rev. B **94**, 174435 (2016).

[27] M. J. Jiménez, A. B. Schvval, and G. F. Cabeza, Ab initio study of FeRh alloy properties, Comput. Mater. Sci. **172**, 109385 (2020).

[28] C. Cazorla and R. Rurali, Dynamical tuning of the thermal conductivity via magnetophononic effects, Phys. Rev. B **105**, 104401 (2022).

[29] Y. J. Hao, L. Zhang, and J. Zhu, The electronic structure, phase transition, elastic, thermodynamic, and thermoelectric properties of FeRh: High-temperature and high-pressure study, Z. Naturforsch. A **75**, 789 (2020).

[30] V. Uhlíř, J. A. Arregi, and E. E. Fullerton, Colossal magnetic phase transition asymmetry in mesoscale FeRh stripes, Nat. Commun. **7**, 13113 (2016).

[31] X. Wu, Z. Liu, and T. Luo, Magnon and phonon dispersion, lifetime, and thermal conductivity of iron from spin-lattice dynamics simulations, J. Appl. Phys. **123**, 085109 (2018).

[32] D. Fournier, M. Marangolo, and C. Frétigny, Measurement of thermal properties of bulk materials and thin films by modulated thermoreflectance (MTR), J. Appl. Phys. **128**, 241101 (2020).

[33] M. Rahimi, K. Sobnath, F. Mallet, P. Lafarge, C. Barraud, W. Daney De Marcillac, Danièle Fournier, and M. L. Della Rocca, Complete determination of thermoelectric and thermal properties of supported few-layer two-dimensional materials, Phys. Rev. Appl. **19**, 034075 (2023).

[34] C. Frétigny, J. P. Roger, V. Reita, and D. Fournier, Analytical inversion of photothermal measurements: Independent determination of the thermal conductivity and diffusivity of a conductive layer deposited on an insulating substrate, J. Appl. Phys. **102**, 116104 (2007).

[35] X. Qian, Z. Ding, J. Shin, A. J. Schmidt, and G. Chen, Accurate measurement of in-plane thermal conductivity of layered materials without metal film transducer using frequency domain thermoreflectance, Rev. Sci. Instrum. **91**, 064903 (2020).

[36] V. Saidl, M. Brajer, L. Horák, H. Reichlová, K. Výborný, M. Veis, T. Janda, F. Trojánek, M. Maryško, I. Fina, X. Marti, T. Jungwirth, and P. Němec, Investigation of magneto-structural phase transition in FeRh by reflectivity and transmittance measurements in visible and near-infrared spectral region, New J. Phys. **18**, 083017 (2016).

[37] S. P. Bennett, M. Currie, O. M. J van 't Erve, and I. I. Mazin, Spectral reflectivity crossover at the metamagnetic transition in FeRh thin films, Opt. Mater. Express **9**, 2870 (2019).

[38] J. A. Arregi, F. Ringe, J. Hajduček, O. Gomonay, T. Molnár, J. Jaskowiec, and V. Uhlíř, Magnetic-field-controlled growth of magnetoelastic phase domains in FeRh, J. Phys. Mater. **6**, 034003 (2023).

[39] A. Rosencwaig and A. Gersho, Theory of the photoacoustic effect with solids, J. Appl. Phys. **47**, 64 (1976).

[40] With α tending to infinity, one recovers the usual expression used in thermoreflectance microscopy (Eq. (10) of Ref. [32]). Ignoring the absorption of the pump beam leads to an overestimate of the thermal conductivity of about 5% when analyzing our data.

[41] C. Frétigny, J.-Y. Duquesne, D. Fournier, and F. Xu, Thermal insulating layer on a conducting substrate. Analysis of thermoreflectance experiments, J. Appl. Phys. **111**, 084313 (2012).

[42] Y. Xian, P. Zhang, S. Zhai, P. Yuan, and D. Yang, Experimental characterization methods for thermal contact resistance: A review, Appl. Therm. Eng. **130**, 1530 (2018).

[43] J.-Y. Duquesne, Thermal conductivity of semiconductor superlattices: Experimental study of interface scattering, Phys. Rev. B **79**, 153304 (2009).

[44] H.-K. Lyeo and D. G. Cahill, Thermal conductance of interfaces between highly dissimilar materials, Phys. Rev. B **73**, 144301 (2006).

[45] J. Zhu, D. Tang, W. Wang, J. Liu, K. W. Holub, and R. Yang, Ultrafast thermoreflectance techniques for measuring thermal conductivity and interface thermal conductance of thin films, J. Appl. Phys. **108**, 094315 (2010).

[46] C. Frétigny, J. Y. Duquesne, and Danièle Fournier, Perturbation of the heat lateral diffusion by interface resistance in layered structures, Int. J. Thermophys. **36**, 1281 (2015).

[47] R. B. Wilson and D. G. Cahill, Anisotropic failure of Fourier theory in time-domain thermoreflectance experiments, Nat. Commun. **5**, 5075 (2014).

[48] J. P. Freedman, J. H. Leach, E. A. Preble, Z. Sitar, R. F. Davis, and J. A. Malen, Universal phonon mean free path spectra in crystalline semiconductors at high temperature, Sci. Rep. **3**, 2963 (2013).

[49] E. Péronne, N. Chuecos, L. Thevenard, and B. Perrin, Acoustic solitons: A robust tool to investigate the generation and detection of ultrafast acoustic waves, Phys. Rev. B **95**, 064306 (2017).

[50] In that case, the transient out-of-plane strain induced by a pulsed laser is measured using time-resolved x-ray diffraction. κ_{FeRh} and R_{th} are obtained simultaneously by fitting the time-dependent thickness-averaged strain variations using a layer-resolved 1D thermal transport model, and a DC measurement of the linear thermal expansion.

[51] P. Ruello, B. Perrin, T. Pézeril, V. E. Gusev, S. Gougeon, N. Chigarev, P. Laffez, P. Picart, D. Mounier, and J. M. Breteau, Optoacoustical spectrum of the metal–insulator transition compound $NdNiO_3$: Sub-picosecond pump–probe study, Phys. B: Condens. Matter **363**, 43 (2005).

[52] Y. H. Ren, X. H. Zhang, G. Lüpke, M. Schneider, M. Onellion, I. E. Perakis, Y. F. Hu, and Q. Li, Observation of strongly damped GHz phonon-polariton oscillations in $La_{0.67}Ca_{0.33}MnO_3$, Phys. Rev. B **64**, 144401 (2001).

[53] Y. S. Touloukian, *Thermophysical Properties of Matter: Thermal Diffusivity* (Plenum Press, New York, 1973).

[54] C. W. Kim, J. I. Cho, S. W. Choi, and Y. C. Kim, *The Effect of Alloying Elements on Thermal Conductivity of Aluminum Alloys in High Pressure Die Casting, in Metallurgy Technology and Materials II*, Advanced Materials Research Vol. 813 (Trans Tech Publications, Wollerau, Switzerland, 2013), pp. 175–178.

[55] G. K. White and S. B. Woods, Thermal and electrical conductivity of rhodium, iridium, and platinum, Can. J. Phys. **35**, 248 (1957).

[56] M. Omini and A. Sparavigna, An iterative approach to the phonon Boltzmann equation in the theory of thermal conductivity, Phys. B: Condens. Matter **212**, 101 (1995).

[57] A. J. H. McGaughey, A. Jain, H.-Y. Kim, and B. Fu, Phonon properties and thermal conductivity from first principles, lattice dynamics, and the Boltzmann transport equation, J. Appl. Phys. **125**, 011101 (2019).

[58] O. Hellman and D. A. Broido, Phonon thermal transport in Bi_2Te_3 from first principles, Phys. Rev. B **90**, 134309 (2014).

[59] J. Kim, R. Ramesh, and N. Kioussis, Revealing the hidden structural phases of FeRh, Phys. Rev. B **94**, 180407(R) (2016).

[60] N. A. Zarkevich and D. D. Johnson, FeRh ground state and martensitic transformation, Phys. Rev. B **97**, 014202 (2018).

[61] M. P. Belov, A. B. Syzdykova, and I. A. Abrikosov, Temperature-dependent lattice dynamics of antiferromagnetic and ferromagnetic phases of FeRh, Phys. Rev. B **101**, 134303 (2020).

[62] O. Hellman, I. A. Abrikosov, and S. I. Simak, Lattice dynamics of anharmonic solids from first principles, Phys. Rev. B **84**, 180301(R) (2011).

[63] O. Hellman and I. A. Abrikosov, Temperature-dependent effective third-order interatomic force constants from first principles, Phys. Rev. B **88**, 144301 (2013).

[64] I. S. Novikov, K. Gubaev, E. V. Podryabinkin, and A. V. Shapeev, The MLIP package: Moment tensor potentials with MPI and active learning, Mach. Learn.: Sci. Technol. **2**, 025002 (2021).

[65] A. V. Shapeev, Moment tensor potentials: A class of systematically improvable interatomic potentials, Multiscale Model. Simul. **14**, 1153 (2016).

[66] Y. Zuo, C. Chen, X. Li, Z. Deng, Y. Chen, J. Behler, G. Csányi, A. V. Shapeev, A. P. Thompson, M. A. Wood, and S. P. Ong, Performance and cost assessment of machine learning interatomic potentials, J. Phys. Chem. A **124**, 731 (2020).

[67] R. Y. Gu and V. P. Antropov, Dominance of the spin-wave contribution to the magnetic phase transition in FeRh, Phys. Rev. B **72**, 012403 (2005).

[68] B. L. Zink, A. D. Avery, R. Sultan, D. Bassett, and M. R. Pufall, Exploring thermoelectric effects and Wiedemann–Franz violation in magnetic nanostructures via micromachined thermal platforms, Solid State Commun. **150**, 514 (2010).

[69] S. Mankovsky, S. Polesya, K. Chadova, H. Ebert, J. B. Staunton, T. Gruenbaum, M. A. W. Schoen, C. H. Back, X. Z. Chen, and C. Song, Temperature-dependent transport properties of FeRh, Phys. Rev. B **95**, 155139 (2017).

[70] E. Mancini, F. Pressacco, M. Haertinger, E. E. Fullerton, T. Suzuki, G. Woltersdorf, and C. H. Back, Magnetic phase transition in iron–rhodium thin films probed by ferromagnetic resonance, J. Phys. D **46**, 245302 (2013).

[71] K. Tanaka, T. Moriyama, T. Usami, T. Taniyama, and T. Ono, Spin torque in FeRh alloy measured by spin-torque ferromagnetic resonance, Appl. Phys. Express **11**, 013008 (2018).

[72] T. Usami, M. Itoh, and T. Taniyama, Temperature dependence of the effective Gilbert damping constant of FeRh thin films, AIP Adv. **11**, 045302 (2021).

[73] F. Mahfouzi and N. Kioussis, Damping and antidamping phenomena in metallic antiferromagnets: An *ab initio* study, Phys. Rev. B **98**, 220410(R) (2018).

[74] H. T. Simensen, A. Kamra, R. E. Troncoso, and A. Brataas, Magnon decay theory of Gilbert damping in metallic antiferromagnets, Phys. Rev. B **101**, 020403(R) (2020).

[75] A. Castets, D. Tochetti, and B. Hennion, Spin wave spectrum of iron-rhodium alloy in antiferromagnetic and ferromagnetic phases, Physica B+C **86-88**, 353 (1977).

[76] L. M. Sandratskii and P. Buczek, Lifetimes and chirality of spin waves in antiferromagnetic and ferromagnetic FeRh from the perspective of time-dependent density functional theory, Phys. Rev. B **85**, 020406(R) (2012).

[77] E. T. Swartz and R. O. Pohl, Thermal resistance at interfaces, Appl. Phys. Lett. **51**, 2200 (1987).

[78] E. T. Swartz and R. O. Pohl, Thermal boundary resistance, Rev. Mod. Phys. **61**, 605 (1989).

[79] X. Gonze, B. Amadon, G. Antonius, F. Arnardi, L. Baguet, J.-M. Beuken, J. Bieder, F. Bottin, J. Bouchet, E. Bousquet, N. Brouwer, F. Bruneval, G. Brunin, T. Cavignac, J.-B. Charraud, W. Chen, M. Côté, S. Cottenier, J. Denier, G. Geneste *et al.*, The ABINITproject: Impact, environment and recent developments, Comput. Phys. Commun. **248**, 107042 (2020).

[80] P. Reddy, K. Castelino, and A. Majumdar, Diffuse mismatch model of thermal boundary conductance using exact phonon dispersion, Appl. Phys. Lett. **87**, 211908 (2005).

[81] Note that in the DMM, the orientation around the axis normal (rotation of FeRh by 45° in our case) is not taken into account.

[82] H. T. Huang, M. F. Lai, Y. F. Hou, and Z. H. Wei, Influence of magnetic domain walls and magnetic field on the thermal conductivity of magnetic nanowires, Nano Lett. **15**, 2773 (2015).

[83] A. M. Hofmeister, Thermal diffusivity and thermal conductivity of single-crystal MgO and Al_2O_3 and related compounds

as a function of temperature, Phys. Chem. Miner. **41**, 361 (2014).

[84] This is a decent approximation given the weak temperature dependence of a measured experimentally by Arregi *et al*. [17].

[85] B. Perrin, *Microscale and Nanoscale Heat Transfer*, edited by S. Volz, Topics in Applied Physics Vol. 107 (Springer, Berlin, 2007).

[86] D. Ourdani, A. Castellano, A. K. Vythelingum, J. A. Arregi, V. Uhlíř, B. Perrin, M. Belmeguenai, Y. Roussigné, C. Gourdon, M. J. Verstraete, and L. Thevenard, Experimental determination of the temperature- and phase-dependent elastic constants of FeRh, Phys. Rev. B **110**, 014427 (2024).

[87] D. Royer and E. Dieulesaint, *Elastic Waves in Solids I: Free and Guided Propagation*, Advanced Texts in Physics (Springer, Berlin, 2000).

[88] J. R. Yates, X. Wang, D. Vanderbilt, and I. Souza, Spectral and Fermi surface properties from Wannier interpolation, Phys. Rev. B **75**, 195121 (2007).

[89] F. Knoop, N. Shulumba, A. Castellano, J. P. A. Batista, R. Farris, M. J. Verstraete, M. Heine, D. Broido, D. S. Kim, J. Klarbring, I. A. Abrikosov, S. I. Simak, and O. Hellman, TDEP: Temperature dependent effective potentials, J. Open Source Software **9**, 6150 (2024).

[90] J. P. Perdew, K. Burke, and M. Ernzerhof, Generalized gradient approximation made simple, Phys. Rev. Lett. **77**, 3865 (1996).

[91] P. E. Blöchl, Projector augmented-wave method, Phys. Rev. B **50**, 17953 (1994).

[92] F. Jollet, M. Torrent, and N. Holzwarth, Generation of projector augmented-wave atomic data: A 71 element validated table in the XML format, Comput. Phys. Commun. **185**, 1246 (2014).

[93] A. P. Thompson, H. M. Aktulga, R. Berger, D. S. Bolintineanu, W. M. Brown, P. S. Crozier, P. J. in ’t Veld, A. Kohlmeyer, S. G. Moore, T. D. Nguyen, R. Shan, M. J. Stevens, J. Tranchida, C. Trott, and S. J. Plimpton, LAMMPS—A flexible simulation tool for particle-based materials modeling at the atomic, meso, and continuum scales, Comput. Phys. Commun. **271**, 108171 (2022).

[94] Y. Yang, L. Zhao, D. Yi, T. Xu, Y. Chai, C. Zhang, D. Jiang, Y. Ji, D. Hou, W. Jiang, J. Tang, P. Yu, H. Wu, and T. Nan, Acoustic-driven magnetic skyrmion motion, Nat. Commun. **15**, 1 (2024).